

Towards a Laser-Integrated Module for Marker-Free Sorting of Micrometer-Sized Particles in Microfluidic Channels

Wolfgang Schwarz

In recent years, microfluidic devices have become important tools for cell analysis in biology and medicine. They enable fast and inexpensive analysis with reduced consumption of analytes. However, for optical detection involving FACS (fluorescence-activated cell sorting), sample preparation by attaching an antibody-labeled fluorochrome to the cell is required. Cell tagging by fluorochromes is a mature technology but might affect cell viability and function. In this article we present a novel concept for marker-free detection and first realization steps. We show the integration of a microfluidic chip and an electrically pumped GaAs-based oxide-confined VECSEL (vertical-extended-cavity surface-emitting laser). Particles in the microchannel flow through the laser resonator and induce a change of the cavity resonance, thus allowing sensitive detection to trigger a subsequent sorting process.

1. Introduction

For gas sensing, locking a laser to an atomic transition line, or detecting biological samples, a single-pass scheme is most commonly used [1–3]. Here the optical field is absorbed or scattered during a single encounter with the sample under test.

The cross-section can be enhanced if the sample is part of an optical resonator, as demonstrated for THz spectroscopy [4] and for passive optical resonators [5,6]. Here, the emission from a remote optical source with a broad spectrum is filtered by the cavity and spectrally analyzed. The drawback of this configuration is the low power efficiency, since the major part of the optical excitation is dumped before being detected. An interesting approach with an active resonator was presented by Paul Gourley and dates back to more than a decade ago [7]. The optical cavity was formed by two planar distributed Bragg reflectors (DBRs). An optically pumped active region was embedded between the mirrors which provided optical gain. By injection of a cell into the intermediate microfluidic channel, the cavity's multiple transversal resonances were confined by the gradient refractive index profile of the cell. This scheme demonstrated the discrimination between astrocytoma tumor cells and astrocytes by analysis of the spatially distributed emission spectrum of the cavity.

In contrast, the presented sensor makes use of an electrically pumped active region, which has major benefits for practical applications: (i) the electrical interface allows for integration with other electronics and for instant operation without cumbersome alignment of

the pump laser spot, (ii) the potential of array fabrication with simultaneous operation of multiple active regions enables parallel sensing, and (iii) the direct access to the active region supports additional sensing features like online monitoring of the laser threshold and analysis of self-heterodyne beats giving information on the flow velocity in the microfluidic channel [8].

If a sample is introduced into the standing-wave pattern inside the extended cavity it affects the laser mode and changes of the beam shape and of the emission wavelength are induced. The detection of the beam shape can be realized by an image sensor. Image processing is done to extract the modal pattern. Signal processing algorithms like multidimensional fast Fourier transform (FFT) have a $O(N\log N)$ complexity [9], with N being the number of image points. In a typical image, N can exceed 10^5 . Unlike the beam shape, the spectrum can be optically analyzed by a grating in a parallel fashion. The resulting signal can be captured by a single line of a charge-coupled device (CCD) with $N \approx 10^3$. Thus, evaluation is much faster, which is a favorable advantage in high-throughput applications with frame rates in excess of 1 kHz.

As shown in Fig. 1, the sensor consists of three functional elements: (i) the customized vertical-cavity surface-emitting laser (VCSEL) soldered to a structured heat sink, (ii) the concave surface of the external mirror which is coated with a dielectric distributed Bragg reflector (DBR), and (iii) a microfluidic channel carrying a suspension of the particles to be analyzed.

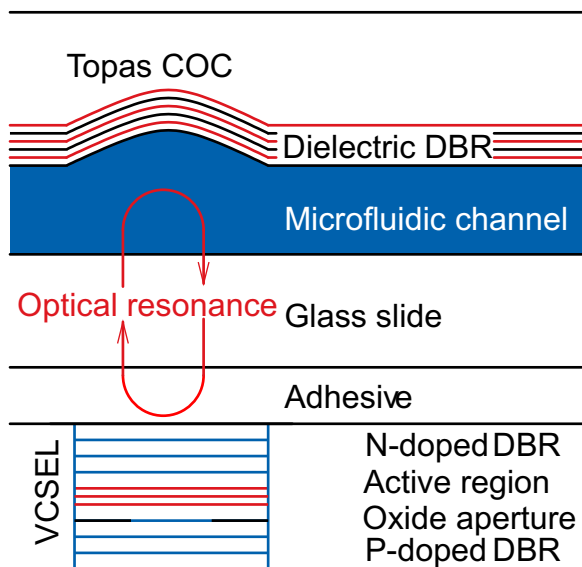


Fig. 1: Schematic drawing of the resonator structure. It comprises the VCSEL at the bottom, the microfluidic channel, and the concave-shaped Topas[®] COC channel wall, which is coated with a dielectric DBR to form the resonator mirror. Electrical contacts and the heat sink are omitted.

2. Fabrication Steps

This section describes the fabrication of the elements in detail. The requirement of a short extended resonator including a microfluidic channel puts tight constraints onto the fabrication procedure: Bond wires are too thick to interface the device electrically. Thus, flip-chip mounting including removal of the substrate is the only reasonable approach

allowing to shrink the cavity length. Since a multitude of fabrication and mounting techniques is employed and the used materials partially have contradictory thermal and mechanical requirements, the choice of materials and mounting sequence is challenging.

On the flip-chip mounted part, both cathode and anode are accessed from the epitaxial side of the wafer. Thus, n-contact and p-contact are structured and equipped with solder bumps for mounting. To prevent diffusion of the solder metal to the fan-out, all possible diffusion paths are blocked by a diffusion barrier.

2.1 VCSEL and heat sink

The VCSEL was grown by molecular beam epitaxy (MBE) on a [100]-oriented n-doped GaAs substrate. The n-doped and p-doped DBRs consist of 10 and 30 periods of AlGaAs, respectively, with an Al content varying between 0.2 and 0.9. After substrate removal, any aluminum-containing surfaces are prone to corrosion. Therefore the phase matching layer beneath the n-doped DBR is terminated by GaAs which is sufficiently chemically stable. However, this layer absorbs light with wavelengths shorter than 870 nm by a fraction of approximately 10^{-3} nm^{-1} , which is unreasonably high for being part of an optical resonator with an enhanced field at this layer. For this reason, the layer structure was designed for a laser emission wavelength from 940 nm to 980 nm, requiring strained indium-containing quantum wells in the active region. Strain compensation by phosphorus was applied in the barriers of the three $\text{In}_{0.16}\text{Ga}_{0.84}\text{As}/\text{GaAs}$ quantum wells.

The schematic cross-section is shown in Fig. 2a. After mesa etching (Fig. 2b), the n-contact was structured on the exposed n-doped DBR by GeAuNiAu evaporation (Fig. 2c) and lift-off. The current injection aperture was formed by selective wet oxidation (Fig. 2d) of an AlAs layer adjacent to the active region. During oxidation, the n-contact was annealed to achieve a low contact resistance. Afterwards, the p-contact (TiPtAu, Fig. 2e) was patterned on top of the mesa via evaporation and lift-off. The exposed surface next to the mesa was planarized with polyimide (Fig. 2f), and gold vias were electroplated to adapt the n-contact to the mesa level (Fig. 2g). A diffusion barrier of 30 nm thick tantalum and 30 nm gold was sputter-deposited on the planarized surface (Fig. 2h). For the subsequent reactive-ion etching (RIE) of the diffusion barrier by argon and tetrafluoromethane (CF_4), 500 nm thick gold was electroplated on mesas and vias as an etch mask (Fig. 2i,j). The processing of the VCSEL part was finalized by wafer thinning (Fig. 2k) and dicing.

The delivery of the electrical pump current to the fluidic VECSEL is crucial. A structured planar piece of silicon was selected to laterally extend the electrical contacts of the mounted VCSEL and to spread the dissipated power. Floating-zone silicon with high resistivity was chosen for the heat sinks because of its beneficial electrical and thermal conductivity. On top of a thin layer of aluminum oxide (Al_2O_3), 30 nm tantalum and 30 nm gold were sputter-deposited on the substrate. The metals served as a base layer for electroplating. The transmission lines were defined by electroplating of 1 μm thick gold. Afterwards, the plating base layer was etched by RIE to electrically separate the transmission lines, and the surface was planarized with polyimide. For good bondability and release of strain in the metallization, the wafer was thermally processed at 727 K for

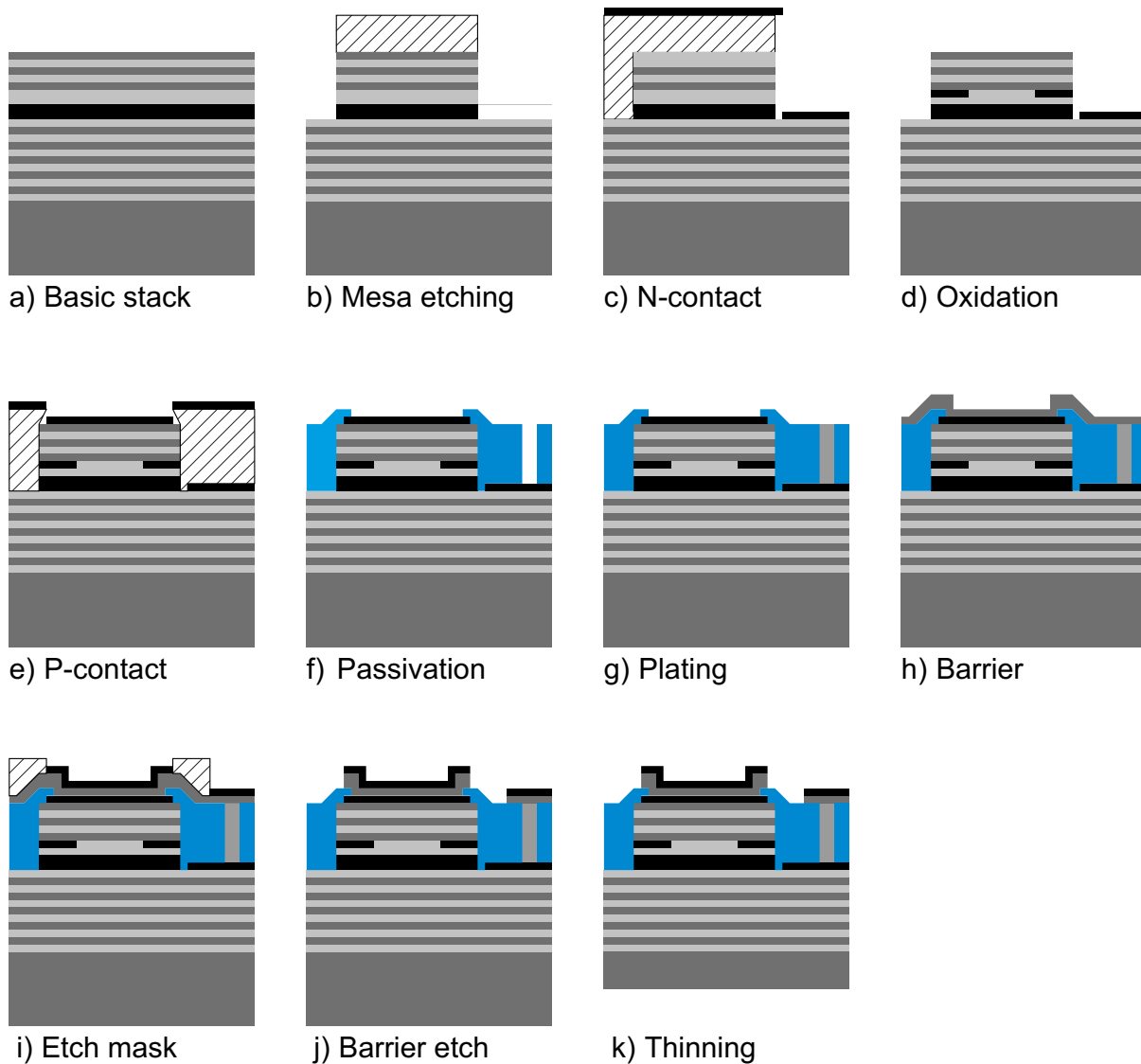


Fig. 2: Processing steps of VCSEL fabrication for flip-chip mounting. The processing of the photoresist (hatched) is simplified; steps like spin coating, photoexposure, development and resist removal are omitted.

10 minutes in nitrogen atmosphere. An insulation resistance reduced to about $80 \text{ k}\Omega$ was recorded after this step, still keeping leakage of the pump current below $30 \mu\text{A}$. Finally, a diffusion barrier was patterned and $5 \mu\text{m}$ thick indium solder bumps were structured by evaporation and lift-off.

The diced VCSEL chips were mounted to the heat sinks by flip-chip soldering at a temperature of 538 K , under assistance of a pressure force of 5 N and formic acid for removal of the native oxides on the solder metal. Care was taken not to overheat the devices, which would result in insulation failures by creation of indium whiskers. The gold surfaces on the VCSELs and on the heat sinks form a soft intermetallic compound with the indium solder. This compound is not prone to embrittlement [10] and reduces the diffusion of solder metal to the gold pads. Due to its mechanical properties, it is well suited for the

mounting of fragile lasers, since it reduces stress originating in the different thermal expansion coefficients of laser substrate and heat sink. The GaAs substrate of the VCSEL was removed by spray etching with a solution of ammonium hydroxide (NH_4OH) and hydrogen peroxide (H_2O_2). When mixed to a pH value of 8.3, the GaAs etchant is highly selective with increasing aluminum content of AlGaAs, and the etching process stops after complete substrate removal at the AlAs layer which is grown prior to the VCSEL structure and serves as an etch stop layer. The remaining part of the n-doped VCSEL mirrors (Fig. 3) is literally brittle and stabilized during the substrate removal by carefully underfilling the gap between VCSEL chip and heat sink with Loctite[®] 3593[™].

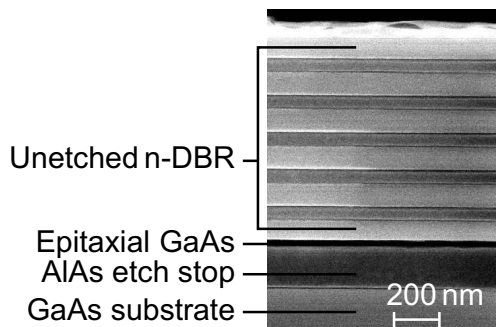


Fig. 3: Cross-section scanning electron micrograph of the remaining layer stack after mesa etching, containing the unetched part of the n-doped DBR, the etch stop layer and the substrate.

The mounted VCSELs are shown in Fig. 4. By means of 36 wire-bondable pads on the heat sinks, the same number of VCSELs on each chip is individually addressable with a processing yield of better than 95 %. The different mesa sizes on each chip allow to match the active diameter of the VCSEL to the radius of curvature of the microfluidic resonator mirror.

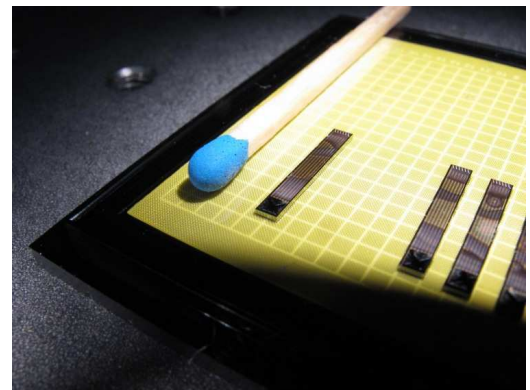


Fig. 4: Photograph of VCSEL chips soldered to the tips of structured heat sinks (approx. $1.88 \times 12.3 \text{ mm}^2$). Each chip accommodates 36 individually addressable lasers with different active diameters.

2.2 External mirror and microfluidic channel

For the design of the external mirror, the radii of curvature in dependence of the distance from the laser were simulated for two different beam sizes assuming Gaussian beam propagation (Fig. 5). We assumed a plane beam front passing the p-DBR, neglecting thermal lensing and other guiding or anti-guiding effects in the VCSEL [11, 12]. The invisible pole at the position $z = 0 \text{ }\mu\text{m}$ is in accordance with the assumed plane beam front at this

point. At the axial position of $20\ \mu\text{m}$, the air/glass boundary shifts the radius of curvature towards a larger radius. An opposite shift is introduced at the glass/channel boundary at $z = 50\ \mu\text{m}$. For a stable resonator, the concave extended mirror should match the radius of curvature of the beam front. The radii of curvature of the fabricated external mirrors range from about $160\ \mu\text{m}$ to $290\ \mu\text{m}$ and allow stable resonator modes for beam waists of $8\ \mu\text{m}$ and $10\ \mu\text{m}$ at the VCSEL part. The diameter of the mirror aperture was designed in such a way that less than 10^{-3} relative power of the fundamental mode is cut by the aperture.

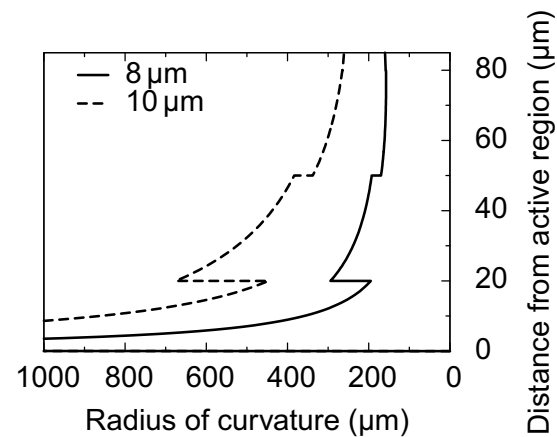


Fig. 5: Calculated radii of curvature of the wavefronts in the extended resonator for two different beam waist sizes. The beam propagates bottom up.

The external mirrors and the microfluidic channels were fabricated by hot embossing of the cyclo-olefin-copolymer Topas[®] COC 5013. From the existing micro-molding techniques, hot embossing enables the fabrication of high precision and high quality polymer micro-structures and is mainly used for optical applications where high accuracy in the geometrical dimensions and a very low surface roughness are required [13]. With this molding technique, a roughness $R_a < 15\ \text{nm}$ and a high contour accuracy could be achieved. Topas[®] COC material was chosen for its low birefringence and high transparency. Contrary to polymethylmethacrylate (PMMA), its low water absorption prevents swelling in water and it supports the deposition of stable dielectric mirrors with thicknesses up to a few micrometers, which is important for the present application. Figure 6 depicts the embossed channels. The channels are $30\ \mu\text{m}$ high and have additional inputs for injection of a sheath fluid to center the particles with respect to the channel [14], which is important for a reproducible response of the sensor. In the region of the resonator mirrors, the channel walls are coated with a dielectric DBR via a shadow mask. Since the DBR is transparent for visible light, only the outer parts of the mirror coating with thinner layers and thus lower Bragg wavelength appear as a bright halo.

Optical layer systems as required for highly reflecting and partially transparent mirrors typically consist of several periods of high and low refracting dielectrics with an overall thickness of several micrometers. If such a system is deposited on a polymer substrate, the maximum layer thickness is limited by the adhesion of the dielectric to the substrate and by mechanical stress building up during deposition. The deposition of thick layer stacks on polymer substrates was rarely reported [15]. By reactive-ion-beam sputter-deposition of oxides of aluminum and tantalum, mirror reflectivities in excess of 98 % have been realized with good adhesion to Topas[®] COC and fair adhesion in case of a microfluidic ambience.

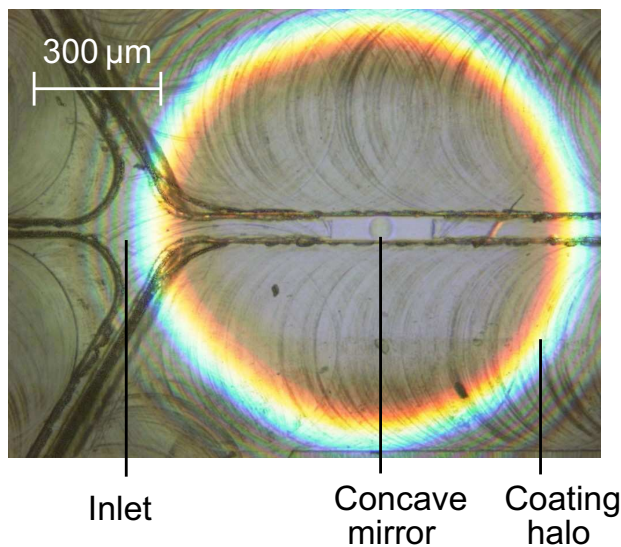


Fig. 6: Optical confocal microscope image of a molded fluidic channel with a concave resonator mirror, coated with a dielectric DBR.

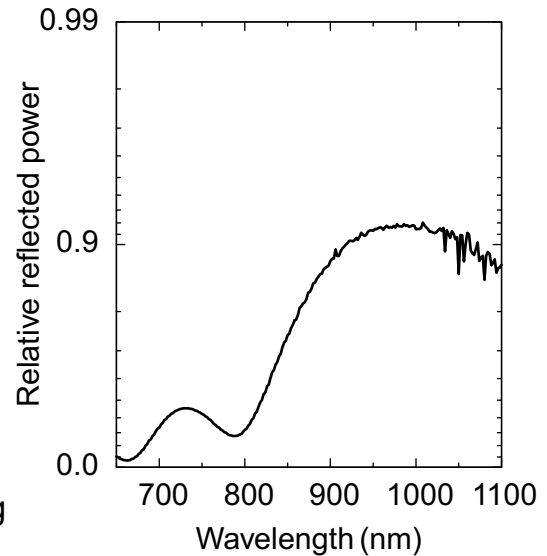


Fig. 7: Measured power reflectivity spectrum of a DBR with 5.5 periods of $\text{Ta}_2\text{O}_5/\text{SiO}_2$ for a reflectivity of 93%. The measurement was done on a coated BK7 glass.

The reflectivity measurement in Fig. 7 was done on a coated BK7 glass as a reference sample. In the present case, the curved surface was coated with 5.5 periods of $\text{Ta}_2\text{O}_5/\text{SiO}_2$ to attain a reflectivity of 93%. With proper surface preparation, this coating has proven to be extraordinary reliable even after weeks of operation in microfluidic ambience. After mirror deposition, the channel is closed vertically by a $30\ \mu\text{m}$ thin glass slide which is fixed by a photocurable adhesive. As a last step, the VCSEL is forward biased, actively aligned to the concave-shaped mirror for laser operation and again fixed by a photocurable adhesive.

3. Operation Characteristics of the Microfluidic VECSEL

The light–current (LI) characteristics of an integrated microfluidic VECSEL with about $15\ \mu\text{m}$ active diameter is shown in Fig. 8. The emission spectra at 7 mA and 10 mA driving current are depicted in Fig. 9. Between 7 mA and 10 mA, the output power is non-monotonic. This transition is accompanied by a hop of the longitudinal mode order with a longitudinal mode spacing of about 1.8 nm. Fundamental transverse operation below and above the hopping point is indicated by low M^2 factors, which were measured to be 1.28 and 1.21 at 7 mA and 10 mA driving current, respectively.

4. First Experiments With Microfluidic Flow

The microfluidic channel was supplied with a flow of 10 nl/s by a precision syringe pump. The emission spectra of the VECSEL were recorded by a linear CCD attached to a

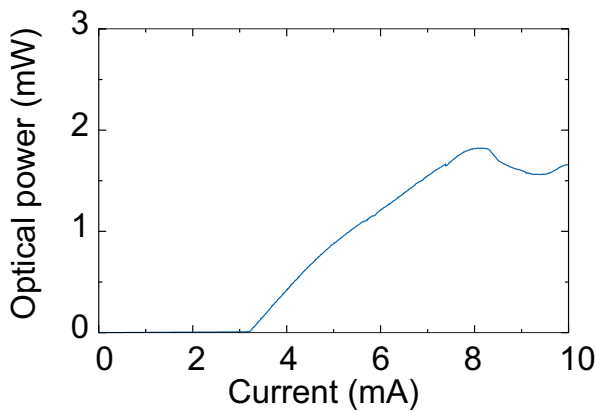


Fig. 8: LI characteristics of a fully functional microfluidic VECSEL.

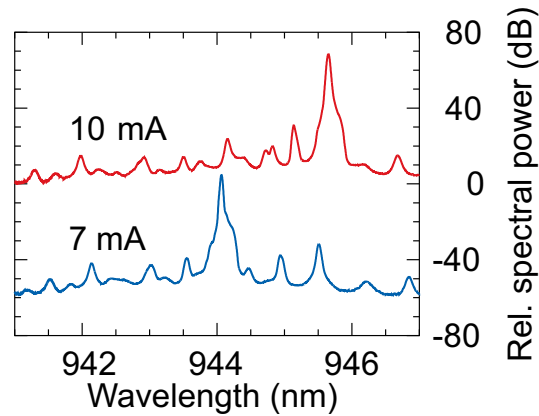


Fig. 9: Emission spectra of a the VECSEL from Fig. 8 at two different driving currents.

monochromator. The monochromator has a Czerny–Turner configuration and 1 m focal length.

For an emission wavelength of 940 nm to 950 nm, each element of the CCD corresponds to a spectral increment of 3 pm and almost resembles the resolving power of the monochromator. Figure 10 shows the change in the peak wavelength over the time. At the beginning of the recording, the dominant wavelength peaks periodically by about 300 pm relative to the baseline. When the syringe pump is stopped after 12 s, the flow stops as well as the periodic pattern in the emission wavelength. The following sudden steps in the emission wavelength are attributed to longitudinal mode flips induced by temperature changes of the channel. There is clear evidence that the periodic changes of the emission wavelength before stopping the pump are related to the pulsation of the syringe drive which changes the optical cavity length.

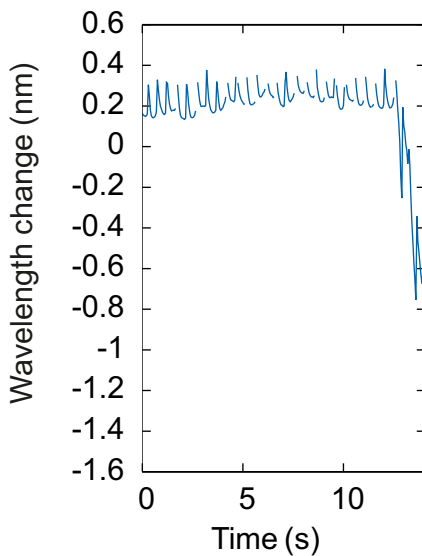


Fig. 10: Time-resolved change of the dominant emission wavelength of the VECSEL. After 12 s, the flow stops as well as the periodic pattern in the emission wavelength. The following discontinuities are attributed to longitudinal mode hops.

5. Conclusion

We demonstrated the concept of an integrated optical sensor. The working principle of the sensor is based on an extended vertical resonator through which the particles flow for detection. Particles passing the resonator are expected to induce a measurable change in the cavity resonance. Details of the fabrication process were presented as well as device characterization and first experiments with water flow inside the microfluidic channel.

The sensor is fully functional. Pulsation of the microfluidic flow could be resolved with a high update rate. Experiments with particle injection into the resonator are in progress and results will be reported in the near future.

Acknowledgment

We thank Antonio Jorge Márquez del Pino for device assembly and measurements, Dieter Rimpf for providing the microfluidic components, Susanne Menzel, Ilona Argut, and Rudolf Rösch for their help with microfabrication, Josef Theisz for fabricating many mechanical parts of the setup, as well as Patrick Herfurth and David Maier for advice on dry etching and flip-chip soldering. This project is financed by the Baden-Württemberg Stiftung gGmbH.

References

- [1] A. Hangauer, A. Spitznas, J. Chen, R. Strzoda, H. Link, and M. Fleischer, “Laser spectroscopic oxygen sensor for real time combustion optimization”, *Procedia Chemistry*, vol. 1, no. 1, pp. 955–958, 2009.
- [2] S. Knappe, “MEMS Atomic Clocks”, Chap. 3.18 in *Comprehensive Microsystems*, Y. Gianchandani, O. Tabata, and H. Zappe (Eds.), pp. 571–612. Amsterdam: Elsevier, 2008.
- [3] P.K. Horan and L.L. Wheelless, Jr., “Quantitative single cell analysis and sorting”, *Science*, vol. 198, no. 4313, pp. 149–157, 1977.
- [4] R. Mendis, V. Astley, J. Liu, and D.M. Mittleman, “Terahertz microfluidic sensor based on a parallel-plate waveguide resonant cavity”, *Appl. Phys. Lett.*, vol. 95, no. 17, pp. 171113-1–3, 2009.
- [5] L.K. Chin, A.Q. Liu, C.S. Lim, X.M. Zhang, J.H. Ng, J.Z. Hao, and S. Takahashi, “Differential single living cell refractometry using grating resonant cavity with optical trap”, *Appl. Phys. Lett.*, vol. 91, pp. 243901-1–3, 2007.
- [6] H. Shao, W. Wang, S.E. Lana, and K.L. Lear, “Optofluidic intracavity spectroscopy of canine lymphoma and lymphocytes”, *IEEE Photon. Tech. Lett.*, vol. 20, pp. 493–495, 2008.

-
- [7] P.L. Gourley, “Biocavity laser for high-speed cell and tumour biology”, *J. Phys. D: Appl. Phys.*, vol. 36, pp. R228–239, 2003.
- [8] A.N. Serov, J. Nieland, S. Oosterbaan, F.F.M. de Mul, H. van Kranenburg, H.H.P.Th. Bekman, and W. Steenbergen, “Integrated optoelectronic probe including a vertical cavity surface emitting laser for laser doppler perfusion monitoring”, *IEEE Trans. Biomed. Engineering*, vol. 53, pp. 2067–2074, 2006.
- [9] M. Frigo and S.G. Johnson, “Design and implementation of FFTW3”, *Proc. IEEE*, vol. 93, no. 2, pp. 216–231, 2005.
- [10] G. Humpston and D.M. Jacobson, *Principles of Soldering*. Materials Park (Ohio): ASM International, 2004.
- [11] G.A. Smolyakov and M. Osiński, “Analysis of ring-metal-aperture VCSELs for single-lateral-mode operation”, *J. Lightwave Technol.*, vol. 23, pp. 4278–4286, 2005.
- [12] L. Raddatz, I.H. White, H.D. Summers, K.H. Hahn, M.R. Tan, and S.-Y. Wang, “Measurement of guiding effects in vertical-cavity surface-emitting lasers”, *IEEE Photon. Technol. Lett.*, vol. 8, pp. 743–746, 1996.
- [13] M. Hecke, W. Bacher, K. D. Müller, “Hot embossing – The molding technique for plastic microstructures”, *Microsystem Technologies*, vol. 4, pp. 122–124, 1998.
- [14] M.L. Shuler, R. Aris, and H.M. Tsuchiya, “Hydrodynamic focusing and electronic cell-sizing techniques”, *Applied Microbiology*, vol. 24, pp. 384–388, 1972.
- [15] U. Schulz, U.B. Schallenberg, and N. Kaiser, “Antireflection coating design for plastic optics”, *Appl. Optics.*, vol. 41, pp. 3107–3110, 2002.